Atomic-matter-wave diffraction evidenced in low-energy $Na^+ + Rb$ charge-exchange collisions

A. Leredde,[1] A. Cassimi,[2] X. Fléchard,[1] D. Hennecart,[2] H. Jouin,[3] and B. Pons[3]
[1]*LPC Caen, ENSICAEN-Université Caen-CRNS-IN2P3, F-14070 Caen, France*
[2]*CIMAP, CEA-CNRS-ENSICAEN, BP5133, F-14070 Caen, France*
[3]*CELIA, Université Bordeaux-CNRS UMR 5107-CEA, F-33400 Talence, France*
(Received 13 December 2011; published 21 March 2012)

Single charge transfer in low-energy $Na^+ + {}^{87}Rb(5s,5p)$ collisions is investigated using magneto-optically trapped Rb atoms and high-resolution recoil-ion momentum spectroscopy. The three-dimensional reconstruction of the recoil-ion momentum provides accurate relative cross sections for the active channels along with their associated distributions in projectile scattering angle. The measurements are accompanied by molecular close-coupling calculations. The predicted diffractionlike oscillations in angular distributions are clearly resolved by the experiment. An excellent agreement is found between the present molecular calculations and the experimental data.

DOI: 10.1103/PhysRevA.85.032710 PACS number(s): 34.10.+x, 34.70.+e

I. INTRODUCTION

Single charge exchange in low-energy ion-atom collisions is quite an old topic which has been extensively studied for decades. Concurrent advances in experimental and theoretical techniques have led to a satisfying knowledge of the underlying dynamics, which is reviewed in textbooks such as [1]. However, the interest in this fundamental process has never faded out since charge exchange plays an important role in astrophysical and Tokamak plasma environments [2,3], ion-induced radiation damage to biological cells [4,5], and many other actual applications. These applications, which cover a wide range of ion impact energies E (from eV to MeV) and involve increasingly complex targets (from atoms to molecules and clusters), continuously show that the charge exchange database is far from being complete.

Moreover, most of the works concerning charge exchange focused on integrated (total) cross sections. In fact, charge exchange occurs at rather large impact parameters so that the scattered projectiles appear strongly peaked about the forward direction. The overlap of scattered and incoming projectile beams thus makes the measurements of angular cross sections difficult. In this respect, the advent of cold-target recoil-ion spectroscopy (COLTRIMS [6]) has been a breakthrough since it allows measurements of differential cross sections with unprecedented resolution. An additional step forward has been achieved as COLTRIMS has been coupled to laser-cooled atomic targets trapped in a magneto-optical trap (MOT) [7–9]. The resulting MOTRIMS setup indeed provides state-selective differential cross sections, with hitherto unsurpassed accuracy, due to the extremely low target cloud temperature. Many experiments have been performed worldwide [7–16], using alkali-metal atomic targets, and have revealed detailed information on single- and multielectron capture processes.

For instance, MOTRIMS experiments have resolved oscillatory patterns in the differential cross sections associated to single charge transfer in low-energy $Li^+ + Na$ collisions [7]. These oscillations have been interpreted in terms of Fraunhofer diffraction of atomic matter waves by analogy with usual diffraction of light waves: The incoming projectile ion, with de Broglie wavelength λ, catches an electron from the target atom provided the impact parameter b is smaller than a typical value b_{max}, so that the target acts as a "hole" of radial aperture b_{max}; angular diffraction patterns with $\lambda/2b_{max}$ characteristic spacing then follow. While diffractionlike oscillations are general features of charge exchange scattering in atomic collisions, their observation has been rather limited so far because of the prohibitive angular resolution required. Even MOTRIMS experiments can fail in this respect, as it has been the case in Ref. [11] for $Na^+ + Rb$ collisions.

In this paper, we revisit $Na^+ + Rb$ collisions in the framework of a joined experimental-theoretical endeavor. A state-of-the-art MOTRIMS setup is employed to obtain relative and differential capture cross sections, not only for dominant channels but also for weak ones. Theoretical calculations using the semiclassical molecular orbital close-coupling (MOCC) scheme are also performed. In this respect, it is interesting to note the interplay between theory and experiment: Theory is needed to gauge whether measurements with given angular resolution can reveal oscillations in charge exchange scattering; on the other hand, refined measurements allows us to test the degree of accuracy of the employed theoretical approach.

Our paper is organized as follows. In Sec. II, we outline the MOTRIMS setup and present the Q-value spectra obtained in $Na^+ + Rb(5s,5p)$ collisions at $E = 0.5$, 2, and 5 keV. The MOCC calculations are described in Sec. III, with particular emphasis on the adequacy of the model potential approach used to describe the collisional systems as effective one-electron systems. State-selective cross-section ratios are given in Sec. IV A and the MOCC calculations are used in Sec. IV B to picture the collision dynamics and therefore understand the magnitudes of the ratios. Computed and measured differential cross sections are compared in Sec. IV C. Finally, we give our conclusions and perspectives in Sec. V. Atomic units are used throughout unless otherwise indicated.

II. EXPERIMENT

The experimental setup has already been described in detail elsewhere [17]. As shown in Fig. 1, it consists of a short ion beam line providing a collimated projectile beam of singly charged alkali-metal particles, a MOT confining the cold target of Rb atoms in a small volume, and a recoil-ion momentum spectrometer (RIMS).

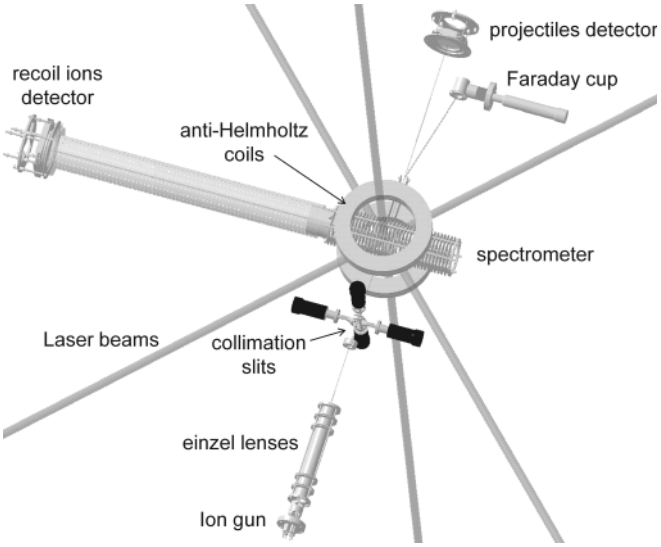

FIG. 1. Schematic view of the experimental setup.

The MOT uses two identical external-cavity diode lasers (DLs) [18], each providing about 100 mW output power at 780 nm. A small fraction of the laser power is sent toward two frequency stabilization systems [19] combining a saturated absorption spectroscopy setup and an acousto-optic modulator. A first laser is tuned a few MHz below the cooling or trapping transition $5\,^2S_{1/2}\ (F=2)-5\,^2P_{3/2}\ (F'=3)$ of the ^{87}Rb atoms; the second is tuned to the repumping transition $5\,^2S_{1/2}\ (F=1)-5\,^2P_{3/2}\ (F'=2)$. The main laser beams are merged through a polarizing beam-splitting cube (PBSC) and sent to a 110-MHz acousto-optic modulator (AOM) used as a fast beam shutter (switch-AOM). The laser beams are then magnified by a two-lens telescope and split into three beams of equal power. The three 14-mm-diameter [full width at half maximum (FWHM)] laser beams enter the trapping chamber along three orthogonal directions and are retroreflected by gold-coated mirrors located on the opposite sides of the chamber. In the trapping volume, they deliver a total power of 65 mW at the cooling or trapping frequency. Six quarter-wave plates ensure the adequate circular polarization for the three pairs of counterpropagating beams. The trapping magnetic-field gradient, of about 20 G/cm in the axial direction, is applied thanks to a 1.8-A current running through two coils arranged in an anti-Helmholtz configuration. A pressure of about 10^{-9} mbar of Rb vapor is maintained in the chamber by heating a cell containing 1 g of natural Rb. The characteristics of the trapped atomic cloud are obtained with a calibrated fast CCD camera. In the experiments described here, we measured a cloud diameter (FWHM) of 0.6 mm and a maximal density of 10^{11} atoms/cm^3. The cloud temperature, $T\sim 200$ K, was determined using the ballistic expansion technique [17].

The Na^+ projectile beam is provided by a homemade thermoionic ion gun. The ions can be accelerated up to 6 keV with a beam energy spread below 0.2 eV. A pair of einzel lenses and two pairs of deflection plates ensure an optimal overlapping of the ion beam with the target. The beam diameter is limited at about 2 mm by two collimators located at the entrance of the trapping chamber to prevent the diffusion of the ions on other elements of the setup. At the exit of the chamber, a set of deflection plates guides the primary beam toward a Faraday cup. Projectiles neutralized by charge exchange with the atomic target are detected by a 40-mm-diameter microchannel-plate position-sensitive detector (MCPPSD) [20]. The instant of their detection serves as a time reference for the recoil-ion time-of-flight (TOF) measurement. The recoil ions produced in the collision region are extracted by the spectrometer electric field toward a similar MCPPSD with 80 mm active diameter. The three components of the recoil momentum are inferred from the position of detection on the MCPPSD and from their TOF. To improve the resolution on the momentum measurement, the spectrometer was designed with an inhomogeneous field region followed by a field-free drift region, which achieves three-dimensional (3D) focusing of the collision region on the detector [17]. In these conditions, the TOF and detection position of the ions do not depend, to first order, on the initial position of the recoil ions within the collision region. The resolution on the momentum measurement is thus here only limited by the performances of the detectors and their electronics, yielding a spatial resolution of 125-μm rms and a TOF resolution of 0.8 ns. In the present work, using an extraction voltage of 20 V, a resolution of about 0.05 a.u. was achieved on the three components of the recoil momentum.

The trapping B field is chopped off during 3 ms at an 80-Hz rate, which allows the detection of collision events whose recoil-ion trajectories are not affected by the trapping magnetic field. During these 3 ms, the trapping and repumping lasers are both switched alternatively 50 μs off and 50 μs on by the switch AOM. In that way, the target is constituted, respectively, either of ^{87}Rb($5s$) atoms or of a mixture of ^{87}Rb($5s$,$5p$) atoms. For each collision event, the position of detection and the TOF of the recoil ion are recorded, as well as the position of the projectile. In addition, the time reference of the collision within the B-field switch cycle, and within the laser switch cycle are sent to the acquisition system. In the data analysis, only the capture events recorded with the B field off are selected. These events are then sorted into two sets, one corresponding to collisions with the lasers off ("lasers off" events) and the other to collisions with the lasers on ("lasers on" events). For each selected event, the Q value and the projectile scattering angle θ are inferred from the recoil-ion momentum components:

$$Q=-\tfrac{1}{2}m_e v_P^2-p_{||}v_P, \tag{1}$$

$$\theta=\frac{p_\perp}{m_P v_P}, \tag{2}$$

where m_e and m_P are, respectively, the mass of the electron and the mass of the projectile, v_P is the projectile velocity, $p_{||}$ and $p_\perp$ are the parallel and perpendicular components of the recoil-ion momentum measured with respect to the initial projectile direction.

Measurements have been performed for $Na^+ + {}^{87}$Rb($5s$,$5p$) collisions with projectile energies of 5, 2, and 0.5 keV. The corresponding Q-value spectra are shown, respectively, in the Figs. 2–4. The lasers on data are shown in the top panels, and the lasers off data (meaning that the target is in the $5s$ ground state) in the middle panels. The electronic configurations nl populated on the scattered projectile are

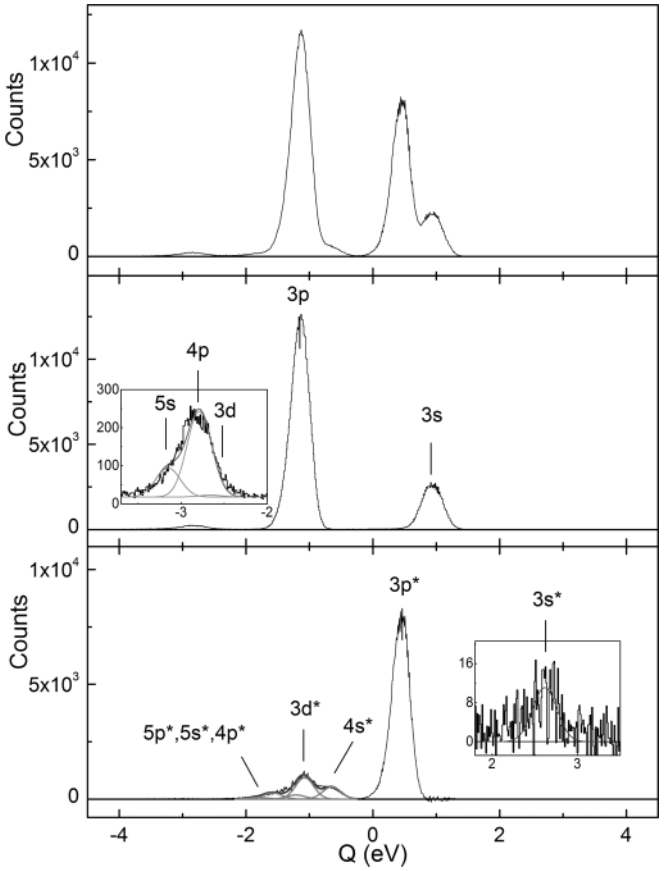

FIG. 2. Q-value spectra for electron transfer in 5-keV Na^+ projectiles colliding with $^{87}Rb(5s,5p)$ (top panel), $^{87}Rb(5s)$ (middle panel), and $^{87}Rb(5p)$ (bottom panel). The configurations (nl) populated on the scattered projectile are labeled on the figures and asterisks indicate channels in which capture is from $Rb(5p)$.

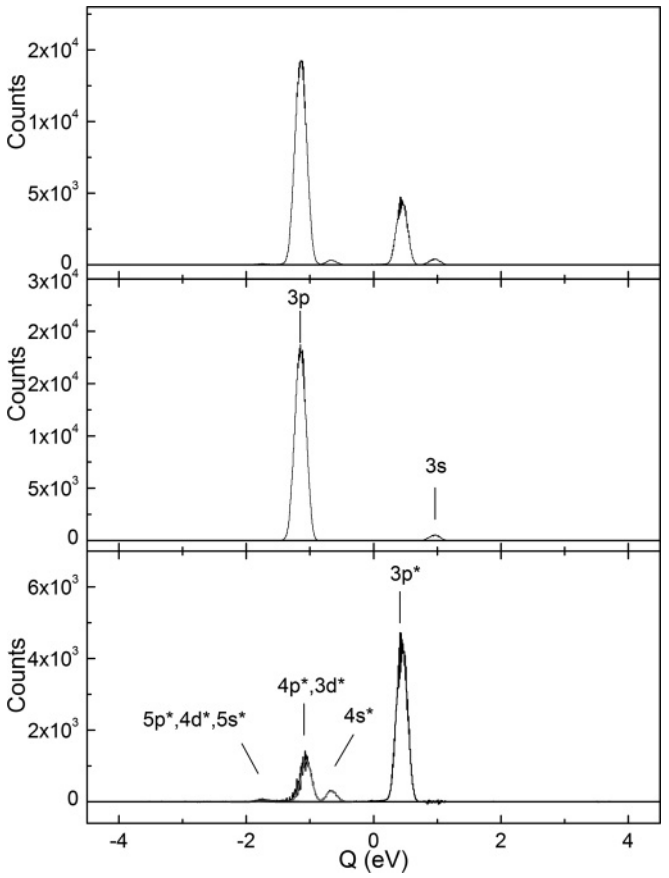

FIG. 3. Same as Fig. 2 but for 2-keV Na^+ projectiles.

labeled on the figures. In the bottom panels, the Q-value spectra are obtained by subtracting from the lasers on events a weighted fraction of the lasers off events in such a way that the contribution of electron capture from the $^{87}Rb(5s)$ ground state is suppressed. The resulting Q-value spectra correspond then to electron capture from ^{87}Rb target only in the $5p$ excited state. The weight w applied to the laser off spectra gives also the excited fraction f of the target in the optical trapping cycle:

$$f = 1 - w. \tag{3}$$

This fraction f depends on the trapping settings such as laser detuning and intensity.

In the case of $Na^+ + {}^{87}Rb(5s,5p)$ collisions at 0.5 keV, the only peak associated with electron capture from $^{87}Rb(5s)$ to $Na(3p)$ can unfortunately be mixed with a small contribution of the $^{87}Rb(5p) \rightarrow Na(3d,4p)$ channels. Therefore, we have determined w and then the excited fraction $f = 0.24 \pm 0.03$ at $E = 0.5$ keV by neglecting the $^{87}Rb(5p) \rightarrow Na(3d,4p)$ contribution, which cannot give an accurate and reliable result. However, for the experiments performed at 2 and 5 keV, w and f were obtained unambiguously by using the $^{87}Rb(5s) \rightarrow Na(3s)$ channel. We found $f = 0.260 \pm 0.003$ for the 2-keV experiment and $f = 0.153 \pm 0.004$ for the 5-keV one.

Knowing these excited fractions, it is straightforward to extract from the data analysis the total capture cross section ratio between $Na^+ + {}^{87}Rb(5p)$ and $Na^+ + {}^{87}Rb(5s)$ collisions

$$R_{5p/5s} = \frac{I_p}{I_s}\frac{1}{f}, \tag{4}$$

where I_p and I_s respectively correspond to the integrals of the Q-value spectra displayed in the bottom and middle panels of Figs. 2–4.

Afterward the relative cross sections for each collision system are obtained by integrating the peaks associated to nl configurations populated on the projectile. When the resolution in Q value does not allow a good separation of the peaks, the spectra are fitted with a combination of Gaussians of fixed positions and widths. The uncertainties obtained on the experimental relative cross sections are purely statistical. They take into account the contribution of the subtraction procedure of laser off data, as well as the error due to the fitting procedure when applied. For 5-, 2-, and 0.5-keV collision energies, the resolutions (rms) obtained on the Q-value measurements are, respectively, $\Delta Q = 137$, 87, and 43 meV.

Doubly differential cross sections in scattering angle are then obtained using Eq. (2) for selections of events associated to the identified electron capture channels. Because of the reconstruction procedure of the transverse recoil momentum component $p_\perp$, making use of both the recoil-ion TOF and position on the detector, the resolution on $p_\perp$ is not as good as on $p_{||}$. It was estimated to be around 0.11 a.u., which

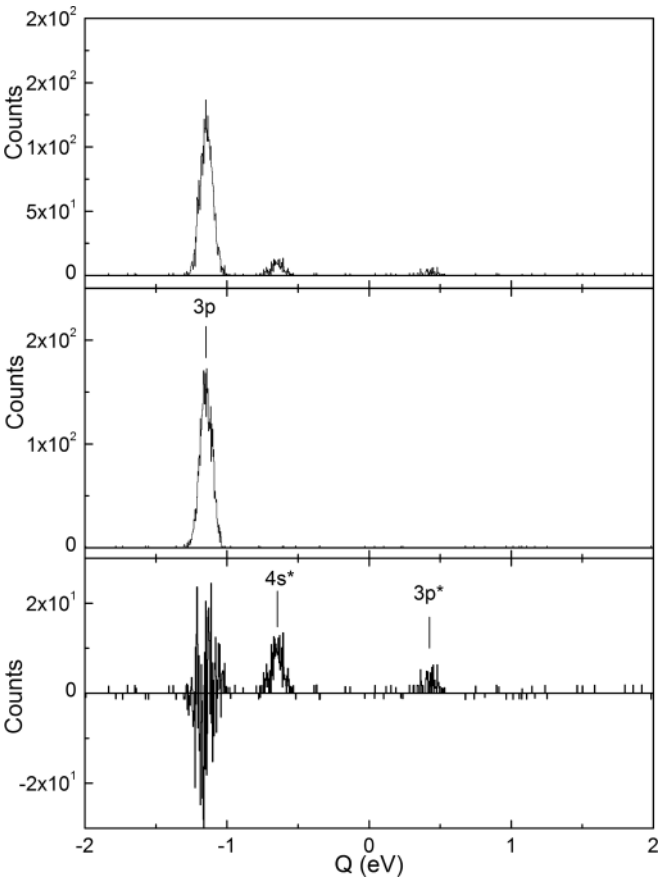

FIG. 4. Same as Fig. 2 but for 0.5-keV Na^+ projectiles.

corresponds to resolutions in scattering angle of $\Delta\theta = 88$, 42, and 28 μrad for 0.5-, 2-, and 5-keV collision energies, respectively.

III. THEORY

As mentioned in the Introduction, our calculations are based on the semiclassical MOCC approach to atomic collisions. We employ the impact parameter approximation [1] in which the projectile follows straight-line trajectories with constant velocity $\mathbf{v}$ and impact parameter $\mathbf{b}$ so that the internuclear vector $\mathbf{R}(t)$ evolves as $\mathbf{R}(t) = \mathbf{b} + \mathbf{v}t$. This approximation has been found to be accurate for impact energies E greater than $\sim$250 eV/amu for prototypical $A^{q+} + \mathrm{H}$ collisions [21,22]; however, we shall see that it can be safely applied down to $E = 0.5$ keV for $Na^+ + Rb$ collisions because of the large projectile and target masses and the long-range electron transitions involved in the main charge exchange processes.

Electron transitions are considered in the framework of the single active electron (SAE) approximation [1] in which the $Na^+[1s^22s^22p^6]$ and $Rb^+[1s^22s^22p^6\cdots 4p^6]$ ionic cores remain frozen throughout the collision. The motion of the active electron, initially bounded to Rb in the $5s$ or $5p$ orbitals, is then quantum mechanically described by the total wave function $\Psi(\mathbf{r},t)$, which is a solution of the eikonal equation

$$i\frac{\partial\Psi(\mathbf{r},t)}{\partial t} = H\Psi(\mathbf{r},t), \tag{5}$$

where $\mathbf{r}$ is the electron position with respect to an origin located on the internuclear axis at distances pR and qR from the target and projectile centers, respectively ($p + q = 1$). The clamped nuclei (Born-Oppenheimer) Hamiltonian H is

$$H = -\frac{1}{2}\nabla^2 + V_{\mathrm{Na}}(r_{\mathrm{Na}}) + V_{\mathrm{Rb}}(r_{\mathrm{Rb}}) + \frac{1}{R}, \tag{6}$$

where $V_{\mathrm{Na}}(r_{\mathrm{Na}})$ and $V_{\mathrm{Rb}}(r_{\mathrm{Rb}})$, with $\mathbf{r}_{\mathrm{Na}} = \mathbf{r} - q\mathbf{R}$ and $\mathbf{r}_{\mathrm{Rb}} = \mathbf{r} + p\mathbf{R}$, are model potentials describing the interaction of the active electron with the Na^+ and Rb^+ ionic cores, respectively, and $1/R$ is the (mean) electrostatic core-core interaction. MOCC thus consists of solving (5) by expanding Ψ on a basis of eigenstates of H. Before presenting this resolution scheme, let us focus on the obtention of the model potentials and associated H eigenstates.

A. Electronic states of the $NaRb^+$ quasimolecule

1. *Optimization of V_{Na} and V_{Rb} model potentials*

$V_{\mathrm{Na}}(r_{\mathrm{Na}})$ and $V_{\mathrm{Rb}}(r_{\mathrm{Rb}})$ present the same analytical form,

$$V(r) = -\frac{1}{r} - (Z-1)\frac{\exp(-b_1 r)}{r} - b_2\exp(-b_3 r), \tag{7}$$

where Z is the nuclear charge ($Z_{\mathrm{Na}} = 11$ and $Z_{\mathrm{Rb}} = 37$) and $\{b_1,b_2,b_3\}$ are parameters which are optimized to reproduce as accurately as possible the valence state energies of the Na and Rb alkali-metal atoms. In practice, the optimization consists of diagonalizing iteratively the atomic Hamiltonians $H_{\mathrm{Na,Rb}}$, which correspond to the molecular H of Eq. (6) in the respective limits ($R \to \infty, r_{\mathrm{Rb}} \to \infty$) and ($R \to \infty, r_{\mathrm{Na}} \to \infty$), with varying parameters $\{b_i\}$ until diagonalization yields eigenenergies that match reference data. In our case, the energies of reference are those tabulated in the NIST Atomic Spectra Database [23], and the atomic Hamiltonians are diagonalized in large-scale "even-tempered" Slater-type-orbitals (STOs) [24],

$$S_j^{(l,m)}(\mathbf{r}) = \mathcal{N}_j^{(l)} r^l e^{-\alpha_j r} Y_l^m(\Omega), \tag{8}$$

where $\mathcal{N}_j^{(l)}$ is a normalization factor and $Y_l^m(\Omega)$ is a spherical harmonic. For all (l,m) angular symmetries, the exponents α_j belong to the geometrical sequence $\alpha_j = \alpha_S\beta_S^j$, with $0 \leqslant j \leqslant j_{\max}$, $\alpha_S = 5\times10^{-4}$, $\beta_S = 1.3$, and $j_{\max} = 50$. We report in Table I the parameters $\{b_i\}$ obtained by means of our optimization procedure for both $Na^+ + e^-$ and $Rb^+ + e^-$ atoms.

In Table II, we compare the energies of our computed Na eigenstates with the reference data taken from NIST [23], putting special emphasis on the states which are significantly populated through charge exchange in low-energy $Na^+ + Rb(5s,5p)$ collisions. One can note a very good agreement between our values and the experimental ones, the largest relative difference between them not exceeding 0.3%. However, we have made additional checks on the accuracy of our model

TABLE I. Parameters of the model potentials of Eq. (7).

	b_1	b_2	b_3
$Na^+ + e^-$	2.810	2.850	2.085
$Rb^+ + e^-$	3.923	5.825	1.333

TABLE II. Na valence electron binding energies (in a.u.) obtained from model potential calculations with STO and OEDM + GTO basis sets (see text) compared to experimental data taken from NIST [23] (only the fine structure energies corresponding to the lowest j value are reported). States indicated in bold correspond to the $R \to \infty$ limit of the molecular states included in the dynamical MOCC calculations.

State	NIST	STO	OEDM + GTO
3s	**−0.188 858**	**−0.188 645**	**−0.188 642**
4s	**−0.071 578**	**−0.071 682**	**−0.071 680**
5s	**−0.037 584**	**−0.037 640**	**−0.037 612**
6s	**−0.023 132**	**−0.023 162**	**−0.023 002**
3p	**−0.111 600**	**−0.111 666**	**−0.111 663**
4p	**−0.050 951**	**−0.051 081**	**−0.051 063**
5p	**−0.029 202**	**−0.029 273**	**−0.029 216**
6*p*	−0.018 923	−0.018 964	−0.018 779
3d	**−0.055 936**	**−0.055 789**	**−0.055 789**
4d	**−0.031 442**	**−0.031 385**	**−0.031 382**
5*d*	−0.020 106	−0.020 078	−0.020 028
4f	**−0.031 268**	**−0.031 251**	**−0.031 250**
5*f*	−0.020 010	−0.020 001	−0.019 953

potential. On one hand, we have considered the model potential proposed by Magnier *et al*. [25], which has the same analytical form as our but differs in the values of b_i parameters. We have found that both model potentials lead to almost identical results, provided the same STO basis (8) is used to diagonalize the atomic Hamiltonian. The largest deviation is found for the 4*d* state, within 0.4% with respect to the value tabulated in Table II. Beyond eigenenergies, we also aimed at checking the accuracy of the computed eigenfunctions. Therefore, we have computed oscillator strengths for a set of 12 dipolar transitions involving collisionally important Na states. Comparison of our results with the reference data tabulated in the frame of the Opacity Project [26] shows that typical relative differences are of some percents, with a minimum of 0.1% for the $3s \to 3p$ transition (which involves the most important Na states from the collisional point of view) and a maximum of 9.1% for the $4p \to 3d$ transition. Analogous calculations using the model potential of Ref. [25] lead to similar relative differences with respect to the reference data of Ref. [26].

In Table III, we present the energies of Rb states obtained by means of our model potential STO calculations. These energies closely agree with the reference data from NIST [23]. However, we have considered, as for Na, alternative model potentials that have been previously used. Lee *et al*. [11] designed a potential with two adjustable parameters that yields Rb eigenenergies in worse agreement with the experimental values than our potential does. For instance, the energy of the Rb(5*p*) state, which corresponds to an entrance channel in the case of excited target $Na^+ + Rb$ collisions, then differs by 8% from the NIST value, whereas this difference decreases down to 1% in the present work. Aymar *et al*. [27] proposed a model potential with the form (7) to which they have added a term to represent core polarization. This yields energies in very nice agreement with those listed in Table III for 5*s*, 5*p*, and 6*s* states but the 4*d* state is shifted by 4.5%. This effect could be ascribed to the explicit account for core polarization effects in the potential. Nevertheless, we have observed that using the model potential of Aymar *et al*. with our large-scale STO basis set (effectively larger than the one used in Ref. [27]) makes the agreement between the calculated and NIST Rb(4*d*) energies worse than the one shown in Table III.

TABLE III. The same as Table II for Rb valence electron binding energies.

State	NIST	STO	OEDM + GTO
5s	**−0.153 507**	**−0.153 468**	**−0.153 395**
6s	**−0.061 776**	**−0.061 780**	**−0.061 757**
7s	**−0.033 623**	**−0.033 647**	**−0.033 606**
8*s*	−0.021 160	−0.021 177	−0.021 079
5p	**−0.096 193**	**−0.095 075**	**−0.095 047**
6p	**−0.045 453**	**−0.045 306**	**−0.045 183**
7p	**−0.026 681**	**−0.026 644**	**−0.026 292**
4d	**−0.065 316**	**−0.064 989**	**−0.064 981**
5d	**−0.036 406**	**−0.036 368**	**−0.036 302**
6d	**−0.022 798**	**−0.022 780**	**−0.022 487**
4f	**−0.031 433**	**−0.031 306**	**−0.031 297**
5f	−0.020 107	−0.020 045	−0.019 983

Besides the close correspondence of our results and NIST reference data presented in Tables II and III, all the convergence checks we have performed allow us to trust on the adequacy and accuracy of our model potentials to represent the interaction of the valence electron with Na^+ and Rb^+ ionic cores in the framework of the SAE approximation.

2. *Molecular eigenstates*

The bound molecular eigenstates χ_k of the $NaRb^+$ quasimolecule, which are used in the MOCC calculations and fulfill

$$H\chi_k(R,\mathbf{r}) = E_k(R)\chi_k(R,\mathbf{r}), \tag{9}$$

cannot be obtained by diagonalizing H in the previous Rb- and Na-centered STO basis sets since the latter are so large that they are prone to linear dependencies for $R \leqslant 10$ a.u. We thus have drawn from previous works on dressed projectile-target interactions [28,29] and decided to diagonalize H in a basis of one-electron diatomic molecule (OEDM) orbitals of $H_2{}^+$, which are eigenfunctions of the Hamiltonian obtained by replacing $V_{\rm Na}(r_{\rm Na})$ and $V_{\rm Rb}(r_{\rm Rb})$ by the net interactions $-1/(r_{\rm Na})$ and $-1/(r_{\rm Rb})$ in Eq. (6). In practice, the OEDM set includes 70 states, which are those asymptotically correlated to $H(n \leqslant 5,l,m)$. However, this basis set is not complete enough to yield an accurate description of the χ_k molecular states, mainly because of the lack of underlying orbitals sharply peaked on the nuclear centers, which are necessary to describe the effect of the ionic cores on the χ_k orbitals. Following [28,29], we accordingly complete the OEDM set by Gaussian-type orbital (GTO) basis sets on both nuclei

$$G_k^{(n_1,n_2)}(\mathbf{r}_{\rm Na,Rb}) = \mathcal{N}_k^{(n_1,n_2)} x_{\rm Na,Rb}^{n_1} z_{\rm Na,Rb}^{n_2} e^{-\alpha_k r_{\rm Na,Rb}^2}, \tag{10}$$

where $x_{\rm Na,Rb}$ and $z_{\rm Na,Rb}$ are the Cartesian coordinates of the electronic vectors $\mathbf{r}_{\rm Na}$ and $\mathbf{r}_{\rm Rb}$ defined in the molecular frame with $\hat{\mathbf{z}}_{||}\hat{\mathbf{R}}$ and $(\hat{\mathbf{x}},\hat{\mathbf{z}}) = (\hat{\mathbf{v}},\hat{\mathbf{b}})$. $\mathcal{N}_k^{(n_1,n_2)}$ is a normalization factor, while n_1 and n_2 are integers such that $0 \leqslant n_1 + n_2 \leqslant 2$. The exponents α_k are taken to form a geometrical sequence of

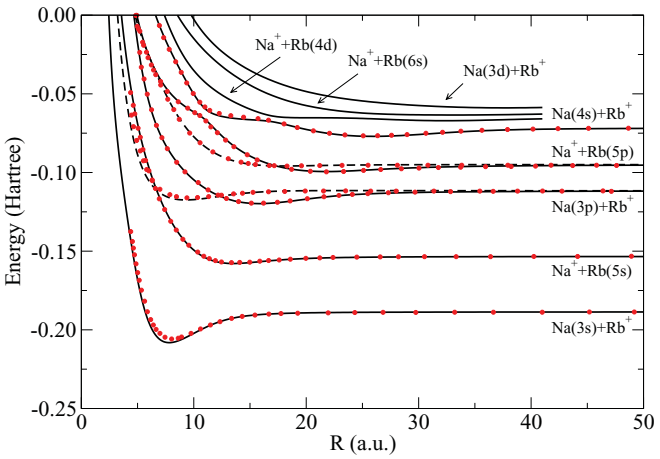

FIG. 5. (Color online) Adiabatic potential energy curves for the 8σ (—) and 2π (- - -) most bounded valence states of the $NaRb^+$ molecule. Lines, present calculations performed by means of the model potentials and the OEDM + GTO basis set; dots, results of Ghanmi *et al.* [30].

rather large numbers $\alpha_k = \alpha_G \beta_G^k$ with $\alpha_G = 0.03$, $\beta_G = 2.5$, and $0 \leqslant k \leqslant 14$ for all the $(n_1 + n_2)$ symmetries considered. The augmented OEDM + GTO basis set then totals 280 states.

The asymptotic energies $E_k(R \to \infty)$ obtained through diagonalization of H in the enlarged OEDM + GTO basis are reported in Tables II and III for the Na and Rb states, respectively. Deviations from the computed STO results are significantly smaller than 10^{-3} a.u.; this indicates the effective completeness of the OEDM + GTO basis set, which succeeds as well as the previous STO basis in providing an accurate description of asymptotic molecular states. Among the 280 molecular states which result from diagonalization, we retain the 42 lower-lying ones, indicated in bold in Tables II and III, for the dynamical calculations. The remaining ones lie too high from the entrance channels on the energy scale to be efficiently populated in the impact energy range $E \leqslant 5$ keV that we consider.

In Fig. 5, we display the correlation diagram of the $Na^+ + Rb$ system, which is the dependence on the internuclear distance R of the molecular energies $E_k(R)$, making special emphasis on the σ and π states which lie closer to the entrance $Na^+ + Rb(5s,5p)$ channels. We compare our results to those of Ghanmi *et al.* [30], who used nonempirical pseudopotentials [31] augmented with core polarization terms [32] to describe the interaction of the valence electron with the frozen ionic cores. One can observe a good agreement between the calculations in the whole range of R's. Importantly, the energy differences in the regions of pseudocrossings between adjacent molecular levels of same symmetry, which tailor the radial collisional dynamics at low impact energies, are similarly described by the model and pseudopotential approaches. Alternatively to our Na model potential, we have also used that of Magnier *et al.* [25] to build the $NaRb^+$ correlation diagram; this has yielded molecular energies $E_k(R)$ indistinguishable from those drawn in Fig. 5 for $R \gtrsim 5$ a.u. This is very satisfactory from a convergence point of view since the $R < 5$ a.u. collisional range cannot be fairly described by any model- or pseudopotentials associated to *frozen* ionic cores. Further, in the dynamical calculations we prevent the system from entering this inner region where the cores overlap and the structure of the $NaRb^+$ quasimolecule is not accurately reproduced.

B. Dynamical calculations

The eikonal equation (5) is solved by expanding the total wave function $\Psi(\mathbf{r},t)$ into the set of 42 molecular orbitals $\chi_k(\mathbf{r},R)$,

$$\Psi(\mathbf{r},t) = e^{iU(\mathbf{r},t)} \sum_{k=1}^{42} a_k(v,b;t)\chi_k(\mathbf{r},R) e^{-i\int^t E_k(t')dt'}, \quad (11)$$

where $U(\mathbf{r},t)$ is a common translation factor (CTF) [33] which ensures that $\Psi(\mathbf{r},t)$ is Galilei invariant and satisfies the correct asymptotic conditions. In practice, we have used the CTF defined in Refs. [33,34] in terms of prolate spheroidal coordinates. Introduction of Eq. (11) in Eq. (5) leads to a set of first-order coupled differential equations for the amplitudes $a_k(v,b;t)$,

$$\frac{da_k}{dt} = \sum_m a_m \left(\langle \chi_k | \frac{vt}{R}\frac{\partial}{\partial R} + \frac{b^2}{R^2} i L_y - \frac{1}{2}\nabla^2 U - \nabla U \dot{\nabla} | \chi_m \rangle \right.$$
$$\left. - i \langle \chi_k | \frac{1}{2}(\nabla U)^2 + \frac{\partial U}{\partial t} | \chi_m \rangle \right) e^{-i\int_0^t (E_m - E_k)dt'}, \quad (12)$$

where $\langle \chi_k | \frac{\partial}{\partial R} | \chi_m \rangle$ and $\langle \chi_k | i L_y | \chi_m \rangle$ are known as the radial and rotational couplings [1], respectively. The system (12) is numerically solved from $-t_{\max}$ up to $t_{\max} = 150/v$ subject to the initial conditions $a_k(v,b;-t_{\max}) = \delta_{ik}$, assuming that χ_i is the initial state. For $Na^+ + Rb(5s)$ collisions, χ_i is unique (see Fig. 5). According to our experimental setup, the entry state in $Na^+ + Rb(5p)$ collisions is neither oriented nor aligned so that the initial flux is statistically shared among the $5p\sigma$, $5p\pi^+$, and $5p\pi^-$ states. $Na^+ + Rb(5p)$ collisions thus necessitate three separate resolutions of Eq. (12), and the final dynamical results consists of incoherent sums over these three conditions.

In the center-of-mass (c.m.) frame, the differential cross-section (DCS) associated with the process $i \to f$ depends on the angle $\theta_{\text{c.m.}}$ according to

$$\frac{d\sigma_{i\to f}}{d\theta_{\text{c.m.}}}(v;\theta_{\text{c.m.}}) = \kappa^2 \left| \int_0^\infty db\, b\, F_{\text{cut}}(b) J_{\Delta m}(2\kappa b \sin\theta_{\text{c.m.}}/2) \right.$$
$$\left. \times [t_{i\to f}(v,b) - \delta_{if}] \right|^2, \quad (13)$$

where $\kappa = \mu v$, μ is the reduced mass, $J_{\Delta m}$ stands for the Bessel function of the first kind of order $\Delta m = |m_f - m_i|$, and $t_{i\to f}(v,b)$ is the transition amplitude. This latter is related to the expansion amplitude for the state f at time $t_{\max}$ through $t_{i\to f}(v,b) = a_k(v,b;t_{\max})e^{-i\delta(b)/v}$ where the b-dependent phase $\delta(b)$ is (see [35] for details)

$$\delta(b) = \nu_f(Z_{\max}) + \nu_i(Z_{\max}) - Z_{\max}(\epsilon_f + \epsilon_i)$$
$$- 2Q_T Q_P \ln b + (q_i + q_f)\ln(u), \quad (14)$$

with $Z_{\max} = vt_{\max}$, $u = Z_{\max} + \sqrt{Z_{\max}^2 + b^2}$, $\nu_k(Z_{\max}) = \int_0^{Z_{\max}} E_k(Z')dZ'$, and $\epsilon_k = \lim_{R\to\infty} E_k(R)$. $Q_T = 1$ and $Q_P = 1$ are the target and projectile ionic core charges and q_k

is related to the asymptotic behavior of the k state energy: $E_k(R) \sim \epsilon_k - q_k/R$.

In Eq. (13), we have introduced the cutoff function $F_{\rm cut}(b)$, such that $F_{\rm cut}(b) = 0$ for $b \leqslant 4$ a.u., $F_{\rm cut}(b) = 1$ for $b \geqslant 6$ a.u., and $F_{\rm cut}(b) = b/2 - 2$ otherwise, in order to cancel the contribution of inelastic transitions occurring in the R range where the Na and Rb ionic cores overlap. Even if this contribution is small for the main reaction channels at low v (as one can infer from Fig. 5), its inaccurate description in terms of frozen atomic cores can distort the DCSs at large deflection angles. In the next section, we quantitatively show the effect of $F_{\rm cut}$ on the dynamical results.

We compute the DCS in the laboratory frame from the c.m. one as follows:

$$\frac{d\sigma_{i\to f}}{d\theta}(v;\theta) = \left|\frac{1+2\zeta\cos\theta_{\rm c.m.}+\zeta^2}{1+\zeta\cos\theta_{\rm c.m.}}\right| \frac{d\sigma_{i\to f}}{d\theta_{\rm c.m.}}(v;\theta_{\rm c.m.}), \tag{15}$$

where $\zeta = M_{\rm Na}/M_{\rm Rb} = 0.2644$ is the ratio of atomic masses. In order to perform comparisons with the experimental data, the DCSs are convoluted with a Gaussian function which has a FWHM that corresponds to the experimental resolution $\Delta\theta$.

It is legitimate to ask whether the semiclassical approach that we have described is really appropriate to the description of $Na^+ + Rb$ collisions at impact energies as low as 0.5 keV (which correspond to $v \approx 0.0295$ a.u.). In the full quantum-mechanical framework, the DCS in the c.m. frame is defined by

$$\frac{d\sigma^{(Q)}_{i\to f}}{d\theta_{\rm c.m.}} = \frac{1}{4\kappa^2}\left|\sum_j (2j+1)\sqrt{\frac{(j-\Delta m)!}{(j+\Delta m)!}} \times P_j^{\Delta m}(\cos\theta_{\rm c.m.})\left(S^j_{i\to f}-\delta_{if}\right)\right|^2, \tag{16}$$

where j is the total (electronic + nuclear) angular momentum quantum number, $S^j_{i\to f}$ is the scattering matrix element (see [21] for details), and $P_j^{\Delta m}$ is the associated Legendre function of the first kind. Taking into account that j, which can be expressed as $j = \mu v b$, is very large because of the huge value of μ, $\mu = 33\,398.5$ a.u., we formally show in the following that the semiclassical (13) and quantum (16) expressions of the DCS yield almost equal results, even in the extreme case where $v = 0.0295$ a.u. and $b = 1$ a.u. so that $j \sim 1000$ a.u. We start from Eq. (16) and employ the fact that for $j \gg \Delta m$, $(2j+1)/2 \simeq j$ and $\sqrt{(j-\Delta m)!/(j+\Delta m)!} \simeq j^{-\Delta m}$, to rewrite (16) as

$$\frac{d\sigma^{(Q)}_{i\to f}}{d\theta_{\rm c.m.}} \approx \frac{1}{\kappa^2}\left|\sum_j j^{1-\Delta m} P_j^{\Delta m}(\cos\theta_{\rm c.m.})\left(S^j_{i\to f}-\delta_{if}\right)\right|^2. \tag{17}$$

We now consider the semiclassical expression (13), neglecting $F_{\rm cut}$ for the sake of generality, and make the following assumptions: (i) In collisions involving such heavy target and projectile as the present ones, $\theta_{\rm c.m.}$ is very small so that $\sin(\theta_{\rm c.m.}/2) \approx \theta_{\rm c.m.}/2$, (ii) there is a close correspondence between j and b through $b = j/\mu v$, and (iii) the semiclassical transition amplitude $t_{i\to f}$ can be replaced by its quantum analog $S_{i\to f}$ because of the considerably large target and projectile masses that imply long-range transitions where deviations from classical trajectories can be depreciated. According to this, and discretizing the integration on b in Eq. (13), we obtain

$$\frac{d\sigma^{(SC)}_{i\to f}}{d\theta_{\rm c.m.}} \approx \frac{1}{\kappa^2}\left|\sum_j j J_{\Delta m}(j\theta)\left(S^j_{i\to f}-\delta_{if}\right)\right|^2. \tag{18}$$

Since $j \gg \Delta m$, we can use $J_{\Delta m}(j\theta) \simeq j^{\Delta m} P_j^{-\Delta m}(\cos\theta)$ and $P_j^{-\Delta m}(\cos\theta) = (-1)^{\Delta m}(j-\Delta m)!P_j^{\Delta m}(\cos\theta)/(j+\Delta m)! \simeq (-1)^{\Delta m} P_j^{\Delta m}(\cos\theta) j^{-2\Delta m}$ [36] to finally get

$$\frac{d\sigma^{(SC)}_{i\to f}}{d\theta_{\rm c.m.}} \simeq \frac{1}{\kappa^2}\left|\sum_j j^{1-\Delta m} P_j^{\Delta m}(\cos\theta_{\rm c.m.})\left(S^j_{i\to f}-\delta_{if}\right)\right|^2, \tag{19}$$

which corresponds to the simplified form (17) of the quantum DCS. Additionally to the formal similarities of the quantum and semiclassical forms of the DCS, we explicitly checked that full quantum calculations yield DCSs in close agreement with their semiclassical counterparts in the whole range of impact velocities considered in this work [37].

Finally, the total cross section for process $i \to f$ is obtained by integration of the DCS on θ; this leads to

$$\sigma_f(v) = 2\pi \int_0^\infty F^2_{\rm cut}(b) P_f(v,b;t_{\rm max}) b\, db, \tag{20}$$

where $P_f(v,b;t) = |a_f(v,b;t)|^2$ is the probability which can be displayed for given (v,b) as a function of the scaled time $Z = vt$ to reveal the mechanisms underlying the collisional process $i \to f$.

IV. RESULTS

In this section, we first concentrate on the comparison of MOTRIMS and MOCC ratios of state-selective capture cross sections σ_{nl} to the total cross section $\sigma_{\rm tot} = \sum_{nl}\sigma_{nl}$. The MOCC calculations are then used to reveal the collision dynamics in terms of so-called "histories of collision," which consists of displaying for representative impact parameter b and velocity v the temporal evolution of reaction probabilities. We then turn our attention to the DCS and the ability of our improved MOTRIMS setup to yield the diffraction patterns theoretically predicted.

A. State-selective capture ratios

The experimental state-selective capture ratios in $Na^+ + Rb(5s,5p)$ collisions are listed in Tables IV–VI for $E = 5$, 2, and 0.5 keV, respectively. They are compared to previous MOTRIMS results [11]. Even if good agreement is found for the most populated channels, the present setup, which combines transverse extraction of the recoil ions and switch-off of the trapping magnetic field techniques, leads to a considerable decrease of the background noise (see Figs. 2–4), and, consequently, to smaller error bars in the measured ratios. This also allows the detection of weakly populated capture channels which were not accessible in the previous measurements [11].

Concerning $Na^+ + Rb(5s)$ collisions, it is clear from Tables IV–VI that the main capture output is $Na(3p)$ regardless

TABLE IV. Ratios of (n,l)-partial cross sections to the total capture cross section in 5-keV $Na^+ + {}^{87}Rb(5s,5p)$ collisions. The present MOTRIMS results are compared to previous ones [11].

	MOTRIMS (Present)	MOTRIMS ([11])	MOCC
	$Na^+ + {}^{87}Rb(5s)$		
$3s$	0.1873 ± 0.0022	0.19 ± 0.07	0.1927
$3p$	0.7915 ± 0.0084	0.79 ± 0.29	0.8051
$4s$	0.0007 ± 0.0001		0.0004
$(3d + 4p + 5s)$	0.0205 ± 0.0003	0.02 ± 0.01	0.0017
	$Na^+ + {}^{87}Rb(5p)$		
$3s$	0.0015 ± 0.0001		0.0007
$3p$	0.7959 ± 0.0136	0.82 ± 0.05	0.8184
$3d$	0.0997 ± 0.0037		0.0985
$4s$	0.0525 ± 0.0029	0.08 ± 0.01	0.0595
$4p + 5s$	0.0326 ± 0.0026		0.0130
$4d$	0.0178 ± 0.0023	0.03 ± 0.01	0.0071

of the impact energy E. However, as E increases, the Na($3s$) channel becomes more important and consists of ~19% of the total capture flux at $E = 5$ keV. Such a behavior can be understood with the help of the correlation diagram in Fig. 5: The pseudocrossings between the entrance $Na^+ + Rb(5s)$ and capture $Na(3s,3p\sigma) + Rb^+$ channels are too broad to allow efficient nonadiabatic radial transitions at low v so that capture mainly consists of rotational transitions around $R = 6$ a.u., where the entrance channel crosses the $Na(3p\pi) + Rb^+$ state. As v increases, radial hops become possible in the regions of the previous pseudocrossings, giving rise to capture into Na($3s$) and Na($3p\sigma$) states. Higher-order transitions promote the flux onto more excited capture states Na($3d$,$4s$, ...) but their contributions to the total cross section do not exceed a few percent.

Something similar occurs in $Na^+ + Rb(5p\sigma)$ collisions. At $E = 0.5$ keV, which is prototypical of (very) low impact energies, the $Na^+ + Rb(5p\sigma)$-$Na(3p\sigma) + Rb^+$ and $Na^+ + Rb(5p\pi)$-$Na(3p\pi) + Rb^+$ pseudocrossings are too broad to allow direct radial transitions that would preferentially populate the Na($3p$) states. In the ingoing part of $Na^+ + Rb(5p\sigma)$ collisions, the electronic flux then mostly evolves adiabatically until it reaches the $Na^+ + Rb(5p\sigma)$-$Na(4s) + Rb^+$ pseudocrossing, around $R = 10$ a.u. (see Fig. 5), which is narrow enough to enable significant transitions and leads to the dominant Na($4s$) final population. In $Na^+ + Rb(5p\pi)$ collisions, the $Na^+ + Rb(5p\sigma)$ molecular channel is populated by means of a rotational redistribution of the incident flux before the $Na^+ + Rb(5p\sigma)$-$Na(4s) + Rb^+$ transition region is reached. At $E = 0.5$ keV, counting statistics are low and lead to a blurred Q-value spectrum in the range of excited Na($3d$,$4p$) capture channels (see Fig. 4); therefore, the populations of these excited channels cannot be reliably estimated and all the electron flux that does not end up in the Na($4s$) capture state has been experimentally attributed to the $3p$ capture process. However, the MOCC calculations yield sizable populations of excited Na($3d$,$4p$) shells, even at $E = 0.5$ keV, and do not reproduce the $4s - 3p$ selectivity assumed in the analysis of measurements. As E increases, the counting statistics are enlarged and the agreement between experimental and theoretical ratios is restored; the $3p$ capture channel becomes dominant because of efficient direct interactions between the $Na^+ + Rb(5p)$ and $Na(3p) + Rb^+$ molecular channels and the significant contribution of excited Na($3d$,$4s$) levels to total capture shows up in both experiments and calculations (see Tables IV and V).

Beyond the difficulty inherent in the measurement of state-selective capture ratios associated to high-lying states at low E, the agreement of experimental and MOCC results is generally very satisfactory. However, the present MOCC calculations underestimate the population of the most excited states, whose global contribution to the total capture cross section does not exceed 3%, especially in the case of $Na^+ + Rb(5s)$ collisions. This is due to the cutoff function $F_{cut}(b)$, which prohibits inelastic transitions to high-lying capture states at small b.

Besides capture ratios, MOCC calculations obviously provide absolute cross sections according to Eq. (20). Reasonable agreement has been found with the AOCC results published in Ref. [11] in the case of $Na^+ + Rb(5s)$ collisions. On the contrary, our MOCC calculations yield absolute cross sections in sharp disagreement with the AOCC results of Lee *et al.* in the $Na^+ + Rb(5p)$ case. For instance, Lee *et al.* found Na($3p$) and Na($4s$) cross sections of 94.20 and 10.39×10^{-16} cm^2 at $E = 2$ keV, while our calculations lead to $\sigma_{3p} = 18.51 \times 10^{-16}$ cm^2 and $\sigma_{4s} = 1.03 \times 10^{-16}$ cm^2. The MOTRIMS ratio $R_{5p/5s}$ (4) of total capture cross sections in $Na^+ + Rb(5p)$ and $Na^+ + Rb(5s)$ collisions make it possible to discriminate between correct and uncorrect modeling. If we interpret the sum of σ_{3p} and σ_{4s} as a lower bound of the total capture cross section in $Na^+ + Rb(5p)$

TABLE V. Same as Table IV for 2-keV $Na^+ + {}^{87}Rb(5s,5p)$ collisions.

	MOTRIMS (Present)	MOTRIMS ([11])	MOCC
	$Na^+ + {}^{87}Rb(5s)$		
$3s$	0.0264 ± 0.0003	0.02 ± 0.01	0.0296
$3p$	0.9722 ± 0.0030	0.98 ± 0.05	0.9703
$(3d + 4p + 5s)$	0.0014 ± 0.0001	0.00 ± 0.02	0.0001
	$Na^+ + {}^{87}Rb(5p)$		
$3p$	0.7440 ± 0.0052	0.60 ± 0.14	0.7766
$4s$	0.0494 ± 0.0007	0.08 ± 0.03	0.0431
$3d + 4p$	0.1943 ± 0.0019	0.30 ± 0.16	0.1737
$4d$	0.0123 ± 0.0003	0.02 ± 0.01	0.0024

TABLE VI. Same as Table IV for 0.5 keV $Na^+ + {}^{87}Rb(5s,5p)$ collisions.

	MOTRIMS (Present)	MOTRIMS ([11])	MOCC
	$Na^+ + {}^{87}Rb(5s)$		
$3p$	1.0000 ± 0.0150		0.9998
	$Na^+ + {}^{87}Rb(5p)$		
$3p$	0.2506 ± 0.0498		0.0561
$4s$	0.7494 ± 0.1001		0.7702

collisions, insomuch as Lee *et al.* did not explicitly give the AOCC total cross section, we find that $R_{5p/5s}^{\mathrm{AOCC}} \geqslant 6.46$ at 2 keV, assuming that $\sigma_{3p} + \sigma_{3s}$ is a good estimate of the total capture cross section in $Na^+ + Rb(5s)$ collisions (see Table V). Our MOCC calculations yield $R_{5p/5s}^{\mathrm{MOCC}} = 1.31$ in satisfactory agreement with the MOTRIMS value $R_{5p/5s}^{\mathrm{MOTRIMS}} = 1.15$. The experiment is still in favor of MOCC simulations at 5 keV, where $R_{5p/5s}^{AOCC} \geqslant 6.09$, while $R_{5p/5s}^{\mathrm{MOCC}} = 3.56$ and $R_{5p/5s}^{\mathrm{MOTRIMS}} = 3.95$. The discrepancies between AOCC and MOCC calculations can be easily understood. We indeed mentioned in Sec. III A 1 that the target model potential used by Lee *et al.* yields an atomic energy for the $Rb(5p)$ entry state that differs by 8% from the NIST reference value. The difference between the asymptotic energies of the $Rb(5p)$ and $Na(3p)$ channels is then 0.008 73 a.u. in the work of Lee *et al.*, 0.016 58 a.u. in the present work, and 0.016 13 a.u. in the NIST database. The significant underestimation of the former asymptotic energy difference, which persists at the level of the pseudocrossing between molecular curves, leads to the overestimation of the capture flux from $Rb(5p)$ to $Na(3p)$ and higher-lying states. This points out the need for a careful optimization of the description of core-induced screening effects, as presented in Sec. III A 1.

B. Collision dynamics

The MOCC approach is the adequate framework to understand the collision dynamics and related cross-section ratios beyond the intuitive analysis of the correlation diagram of Fig. 5.

Figure 6 includes the weighted probabilities $bP(b)$ which build, according to Eq. (20), the integrated cross sections. We focus on $Na^+ + Rb$ collisions at $E = 5$ keV, which are particularly interesting since more than one output capture channels are significantly populated. Figure 6(a) corresponds to the case of $Na^+ + Rb(5s)$ that mainly leads to capture into the $Na(3p\pi)$ state around $b = 6$ a.u. and, secondarily, to capture into the $Na(3s)$ state with an oscillatory structured $bP(b)$. Oscillatory patterns also appear in the $bP(b)$ profiles of all capture states in $Na^+ + Rb(5p\sigma)$ and $Na^+ + Rb(5p\pi)$ collisions, as shown in Figs. 6(b) and 6(c), respectively. It is worth recalling that in the quantum framework the probability oscillations are basically related to the dependence on b (for fixed v) of the phases $\exp\{-i\int_0^t [E_m(t') - E_k(t')]dt'\}$ accumulated along the nuclear path $\mathbf{R}(t') = \mathbf{b} + \mathbf{v}t'$ and entering the system of coupled equations (12). In the case of a two-state interaction, these oscillations are generally known as Stueckelberg oscillations [1,38]; in a more general case where initial and final states are coupled through various pathways involving different intermediate states and phase contributions, further interference processes come into play [39–42]. Interestingly, the quantum mechanical (interference) picture has a classical analog [39,40,43]: The probability oscillations are related to the number of swaps the electron experiences between the target and the projectile during the collision; the larger b the lower is the number of possible swaps.

The transition pathways between the initial and final states can be revealed by displaying, for representative impact parameters b, "collision histories," which consist of the temporal evolution of probabilities in course of collision.

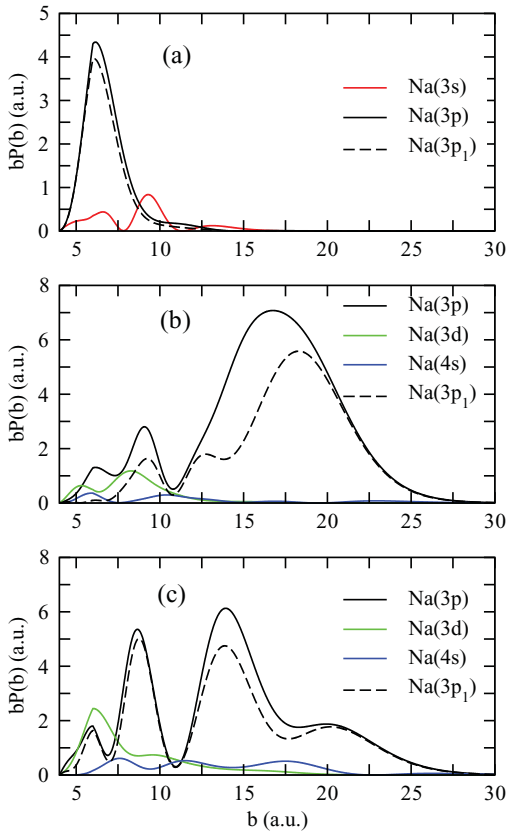

FIG. 6. (Color online) Weighted probabilities $bP(b)$ as functions of the impact parameter b for the most important capture channels (indicated in the figures) in (a) $Na^+ + Rb(5s)$, (b) $Na^+ + Rb(5p\sigma)$ and (c) $Na^+ + Rb(5p\pi)$ collisions for the impact energy $E = 5$ keV.

The case of $Na^+ + Rb(5s)$ collisions is illustrated in Fig. 7 for $b = 9$ a.u. In the incoming part of the collision ($Z < 0$), the $Na(3p\sigma)$ and $Na(3s)$ capture channels are directly populated from the entry state through radial transitions around $Z = -14$ and -8 a.u., corresponding to $R \sim 16$ and 12 a.u., where the respective molecular curves pseudocross (see Fig. 5). Later on, rotational transitions empty the entry channel to populate the $Na(3p\pi)$ level across the distance of closest approach ($Z = 0$ or, equivalently, $R = b = 9$ a.u.). The receding phase of the collision is quite symmetric with respect to the incoming one: direct radial transitions $Rb(5s) \rightarrow Na(3s)$ and $Rb(5s) \rightarrow Na(3p\sigma)$ occur around $R = 12$ and 16 a.u., respectively. It is thus clear that the three main output capture states in low E $Na^+ + Rb(5s)$ collisions, $Na(3s,3p\sigma,3p\pi)$, are directly populated from the entry channel. This can be easily checked in the MOCC framework by canceling artificially the couplings which monitor the transitions. In Fig. 7, we prove that the final $Na(3s)$ and $Na(3p\sigma)$ populations vanish if the respective radial couplings $\langle Na(3s)|\partial/\partial R|Rb(5s)\rangle$ and $\langle Na(3p\sigma)|\partial/\partial R|Rb(5s)\rangle$ are canceled; the same happens for the $Na(3p\pi)$ state if $\langle Na(3p\pi)|iL_y|Rb(5s)\rangle = 0$. As mentioned above, all these direct transitions are amenable to Stueckelberg oscillations in the corresponding $bP(b)$ profiles.

In the incoming part of $Na^+ + Rb(5p\sigma)$ collisions, illustrated in Fig. 8 for $b = 17$ a.u., there is a strong rotational redistribution of the electron flux, $Rb(5p\sigma) \rightarrow Rb(5p\pi)$. Later on, the $Na(3p\sigma)$ and $Na(3p\pi)$ channels are populated as the

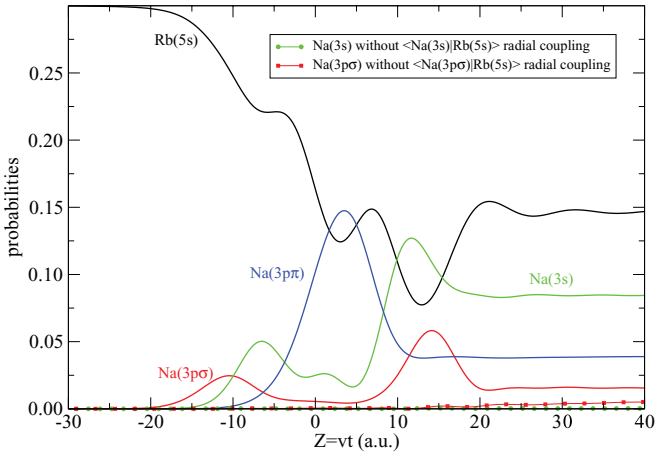

FIG. 7. (Color online) Temporal evolution of probabilities associated to $Na^+ + Rb(5s)$ and $Na(3s,3p\sigma,3p\pi) + Rb^+$ channels in $Na^+ + Rb(5s)$ collisions for $E = 5$ keV and $b = 9$ a.u. The $Na^+ + Rb(5s)$ probability has been shifted down by 0.7 for the sake of clarity. The lines with symbols correspond to probabilities obtained by means of MOCC calculations in which nonadiabatic couplings have been artificially canceled, as indicated in the legend and explained in Sec. IV B.

projectile crosses the target. By canceling successively the rotational $\langle Na(3p\sigma)|iL_y|Rb(5p\pi)\rangle$ and $\langle Na(3p\pi)|iL_y|Na(3p\sigma)\rangle$ couplings, we observe that the main population pathway is $Rb(5p\sigma) \rightarrow Rb(5p\pi) \rightarrow Na(3p\sigma) \rightarrow Na(3p\pi)$. However, when $\langle Na(3p\pi)|iL_y|Na(3p\sigma)\rangle = 0$, secondary radial transitions $Rb(5p\pi) \rightarrow Na(3p\pi)$ operate for $|Z| \lesssim 10$ a.u. when the corresponding molecular curves pseudocross (around $R = 17$ a.u. in Fig. 5). Similarly, when $\langle Na(3p\sigma)|iL_y|Rb(5p\pi)\rangle = 0$, we note remaining radial transitions $Rb(5p\sigma) \rightarrow Na(3p\sigma)$ starting at $Z = -20$ a.u. and a long-range rotational flow $Na(3p\pi) \rightarrow Na(3p\sigma)$ in the receding phase of the collision.

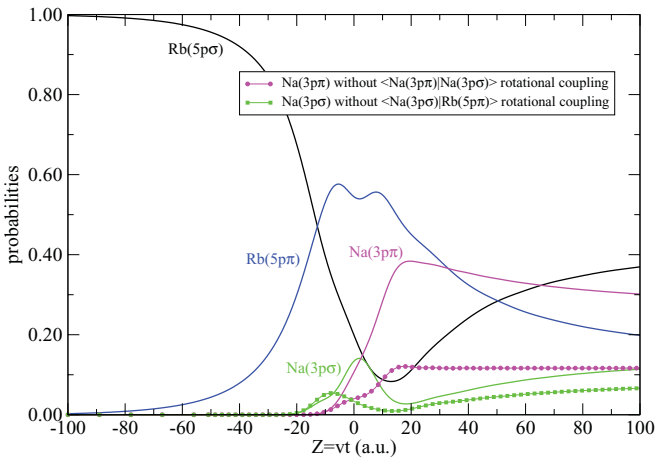

FIG. 8. (Color online) Temporal evolution of probabilities associated to $Na^+ + Rb(5p\sigma,5p\pi)$ and $Na(3p\sigma,3p\pi) + Rb^+$ channels in $Na^+ + Rb(5p\sigma)$ collisions for $E = 5$ keV and $b = 17$ a.u. The lines with symbols correspond to probabilities obtained by means of MOCC calculations in which nonadiabatic couplings have been artificially canceled, as indicated in the legend and explained in Sec. IV B.

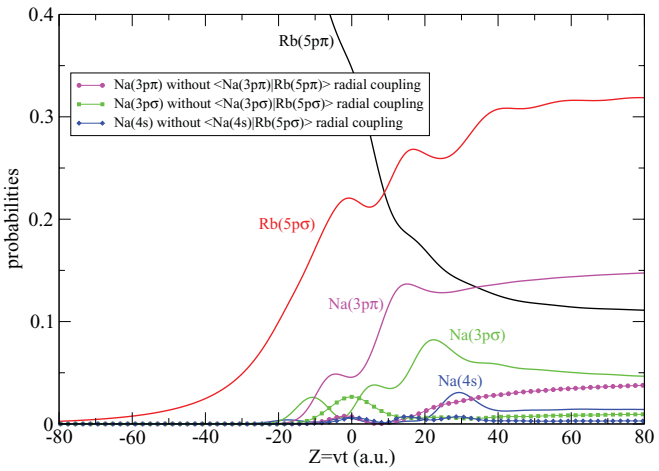

FIG. 9. (Color online) Temporal evolution of probabilities associated to $Na^+ + Rb(5p\sigma,5p\pi)$ and $Na(3p\sigma,3p\pi,4s) + Rb^+$ channels in $Na^+ + Rb(5p\pi)$ collisions for $E = 5$ keV and $b = 13$ a.u. The lines with symbols correspond to probabilities obtained by means of MOCC calculations in which nonadiabatic couplings have been artificially canceled, as indicated in the legend and explained in Sec. IV B.

Both $Na(3p\sigma)$ and $Na(3p\pi)$ are thus populated through multiple pathways which interfere and lead to oscillation patterns, besides pure Stueckelberg ones, in the $bP(b)$ profiles (see Fig. 6).

In $Na^+ + Rb(5p\pi)$ collisions, the dynamics are rather tailored by radial transitions following the initial rotational redistribution of the flux, $Rb(5p\pi) \rightarrow Rb(5p\sigma)$. In Fig. 9, we show by canceling the appropriate couplings that $Na(3p\sigma)$ is populated according to the path $Rb(5p\pi) \rightarrow Rb(5p\sigma) \rightarrow Na(3p\sigma)$, while $Na(3p\pi)$ is mostly populated through direct transitions from the entry channel. On the way out of the collision, a small part of the electron flux is promoted onto higher-lying capture states by means of a ladder-type mechanism involving the $Rb(5p\sigma)$ as first rung and successive radial transitions in the regions of pseudocrossings between adjacent molecular curves, $Rb(5p\sigma) \rightarrow Na(4s) \rightarrow \cdots$.

C. Differential cross sections

Before presenting the comparison of measured and computed state-selective DCSs, it is important to gauge whether the experimental angular resolution makes it possible to detect diffractionlike patterns. Therefore, we present in Fig. 10 the reduced DCS $\sin(\theta)d\sigma/d\theta$ of the capture process $Na^+ + Rb(5s) \rightarrow Na(3s) + Rb^+$ at $E = 2$ keV. Clear oscillations appear in the calculated DCS and Gaussian convolution with $\Delta\theta = 42$ μrad conserves the oscillatory behavior, even though the contrast is significantly reduced. Small peaks in the primary DCS also transform into shoulders in the convoluted DCS whenever those peaks are located in the near neighborhood of main peaks. The measured DCS is superimposed to the calculated ones in Fig. 10(a) to ascertain that the predicted oscillations are effectively detected. Further, we show in the same figure that the angular spacing between adjacent maxima indeed corresponds to the expected diffraction one, $\lambda/2b_{max}$,

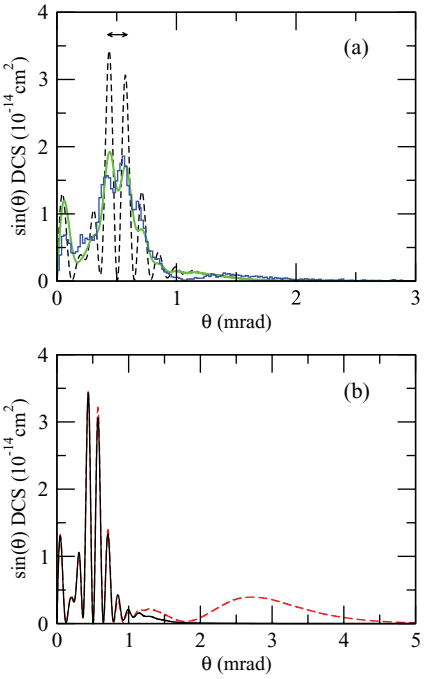

FIG. 10. (Color online) Reduced DCS $\sin(\theta)d\sigma/d\Omega$ for the $Na^+ + Rb(5s) \rightarrow Na(3s) + Rb^+$ capture process at $E = 2$ keV. In (a), we display the MOCC results with (—) and without (- - -) convolution, as well as the result of measurements (histogram); the upper arrow indicates the predicted diffraction spacing between adjacent maxima. In (b), we present the MOCC results involving (—) or not (- - -) the cutoff function $F_{cut}(b)$.

with $b_{max} \sim 11$ a.u. In this respect, our present measurements go beyond previous MOTRIMS experiments on $Na^+ + Rb$ collisions [11].

In Fig. 10(b) we illustrate the effect of the cutoff function $F_{cut}(b)$ introduced in the DCS calculations [see Eq. (13)]. $F_{cut}(b)$ cancels out the contribution of large θ angles to the DCS [$\theta > 2$ mrad in the illustration of Fig. 10(b)]. These large angles are associated with transitions occurring at small internuclear distances, $R < 4$ a.u., where any description of the $NaRb^+$ electronic structure with frozen core atomic model potentials (including our one) is inaccurate. Furthermore, large θ contributions to the DCS do not show up in the measurements; we therefore assume that these contributions are spurious and accordingly prevent their appearance in our computations by means of $F_{cut}(b)$.

In what follows, we separately present the reduced DCS associated to $Na^+ + Rb(5s)$ and $Na^+ + Rb(5p)$ collisions. The calculated and measured DCS have been normalized with respect to each other so that the integrated cross sections, $2\pi \int d\theta \sin(\theta)d\sigma/d\theta$, coincide. Moreover, the reduced DCS are displayed as functions of $E\theta$ since, in a classical picture of scattering, where the trajectory deflection is assumed to be induced by the repulsive Coulomb interaction between the projectile and target cores (of respective charges Q_P and Q_T), small deflection angles are given by $\theta = Q_P Q_T/(Eb)$ in the c.m. frame [44]; transitions occurring at a given impact parameter b thus appear at a fixed $E\theta$ value regardless of E.

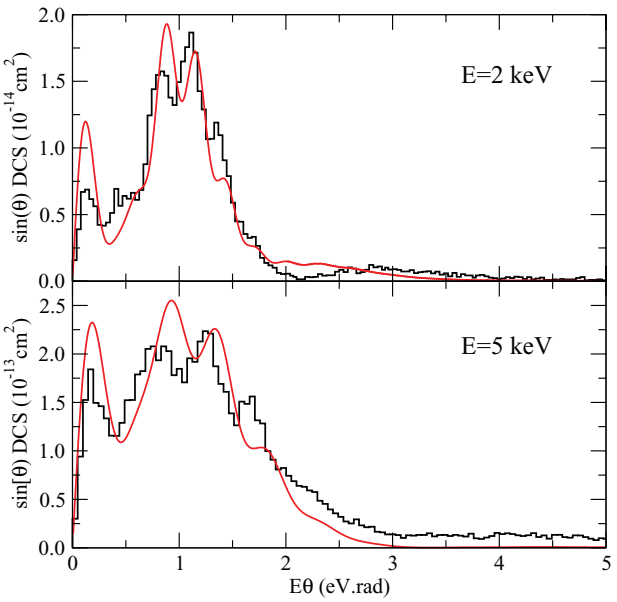

FIG. 11. (Color online) Reduced DCS $\sin(\theta)d\sigma/d\Omega$ for the $Na^+ + Rb(5s) \rightarrow Na(3s) + Rb^+$ capture process at $E = 2$ keV (top) and $E = 5$ keV (bottom). In both cases, the continuous line refers to the convoluted MOCC result and the histogram corresponds to the result of MOTRIMS measurement.

1. $Na^+ + Rb(5s)$ collisions

We report in Fig. 11 the reduced DCS corresponding to the capture process $Na^+ + Rb(5s) \rightarrow Na(3s) + Rb^+$ at $E = 2$ and 5 keV. Counting statistics were insufficient to safely derive an experimental DCS at $E = 0.5$ keV (see Fig. 4). The agreement of MOCC and MOTRIMS DCS is very satisfactory, especially at $E = 2$ keV, where large discrepancies were found in Ref. [11] between theoretical and MOTRIMS results. It should be noted that our present reduced DCS basically reproduce the shape of the $bP(b)$ opacity function of Fig. 6(a): Keeping in mind the classical inverse proportionality of $E\theta$ and b, one can link the three maxima and the shoulder of the $bP(b)$ function to those appearing in the DCS.

In Fig. 12 we notice that no prominent oscillations appear in the DCS associated with charge transfer from $Rb(5s)$ to $Na(3p)$ at $E = 0.5$ keV. This is not an effect of convolution, or alternatively, of inadequate experimental resolution, insomuch as the primary MOCC DCS neither shows diffraction patterns at this energy. Nevertheless, as v increases, the spacing $\pi/\mu v b_{max}$ between diffraction maxima decreases, and our experimental resolution is good enough to allow the observation of nascent oscillations at $E = 5$ keV. We also note that the reduced DCS moves toward smaller $E\theta$ values as E increases. This is because of the increasing contribution of the $3p\sigma$ state to the total $3p$ capture channel; this contribution varies from 3.5% at $E = 0.5$ keV up to 13.3% at $E = 5$ keV, and the $3p\sigma$ DCS peaks at lower θ than the $3p\pi$ one since the former state is populated at larger R (see Fig. 7).

The good agreement found up to now between theoretical and measured DCS disappears as we consider in Fig. 13 charge transfer from $Rb(5s)$ to the sum of excited $Na(4s)$, $Na(3d)$, $Na(4p)$, and $Na(5s)$ states which cannot be experimentally disentangled at $E = 5$ keV (see Fig. 2). The population of

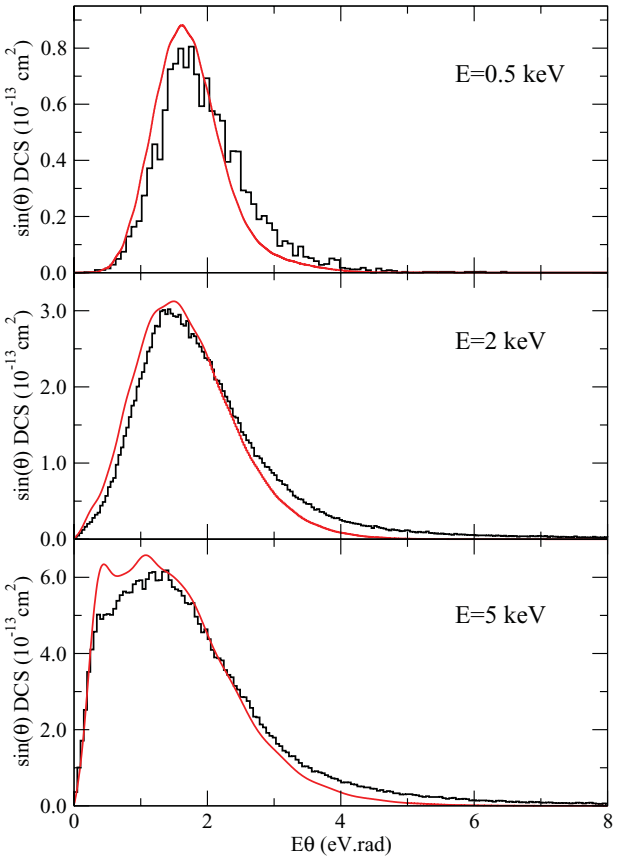

FIG. 12. (Color online) Same as Fig. 11 but for charge transfer from Rb($5s$) to Na($3p$).

these states consist of 2.12% of the total capture flux (see Table IV). Transitions to these high-lying states mostly occur in a range of small impact parameters ($b < 5$ a.u.) that our MOCC calculations involving $F_{\rm cut}(b)$ cannot describe. Calculations without $F_{\rm cut}$ behave better as they yield a maximal DCS around $E\theta = 7$ eV rad; however, they still do not allow to obtain a DCS that merges with the measured one. This illustrates the difficulty to provide, for dressed ion-atom collisions at low E, both accurate DCS for the main capture channels, without spurious contributions at large θ, and accurate DCS for excited states weakly populated at small R. This would necessitate

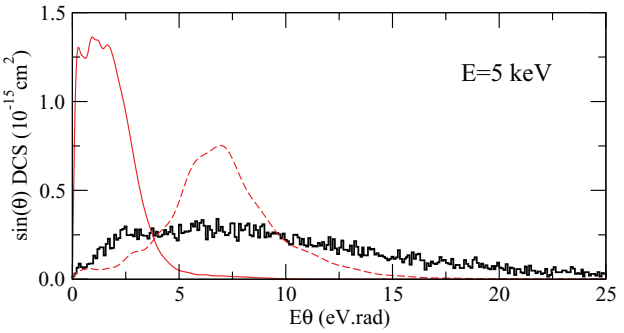

FIG. 13. (Color online) Same as Fig. 11 but for $Na^+ + Rb(5s) \rightarrow Na(4s,3d,4p,5s) + Rb^+$. The dashed line corresponds to MOCC calculations without the cutoff function $F_{\rm cut}(b)$.

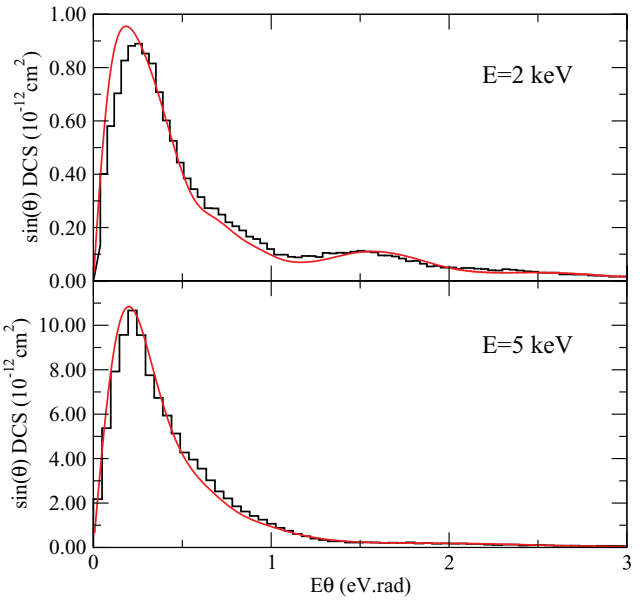

FIG. 14. (Color online) Same as Fig. 11 but for charge transfer from Rb($5p$) to Na($3p$).

the description of the molecularization of the ionic electron cores [45]; this is beyond our skills for such a complex system as $NaRb^+$.

2. $Na^+ + Rb(5p)$ collisions

Counting statistics are too low at $E = 0.5$ keV to derive reliable DCS from the measurements in $Na^+ + Rb(5p)$ collisions. We shall therefore focus on results for $E = 2$ and 5 keV.

We present in Fig. 14 the DCS for charge transfer into the main Na($3p$) channel. A remarkable agreement is found between the computed and measured data. The comparison of Figs. 12 and 14 shows that the present DCS peak at smaller θ

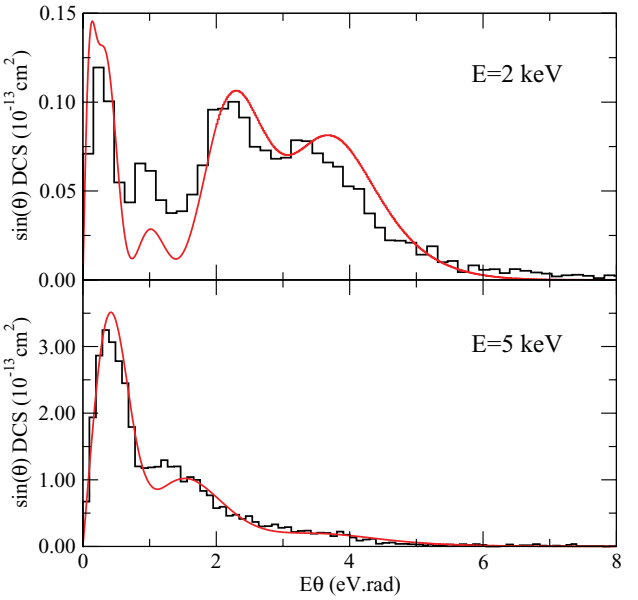

FIG. 15. (Color online) Same as Fig. 11 but for charge transfer from Rb($5p$) to Na($4s$).

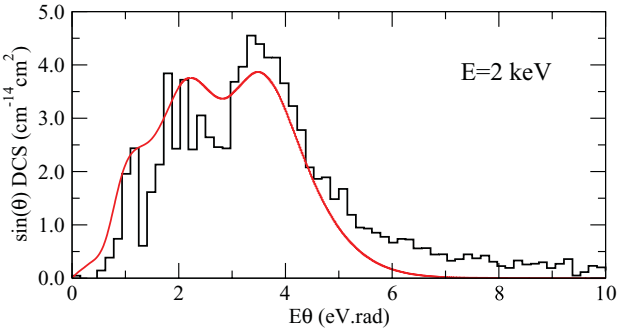

FIG. 16. (Color online) Same as Fig. 11 but for charge transfer from Rb($5p$) to Na($3d$,$4p$).

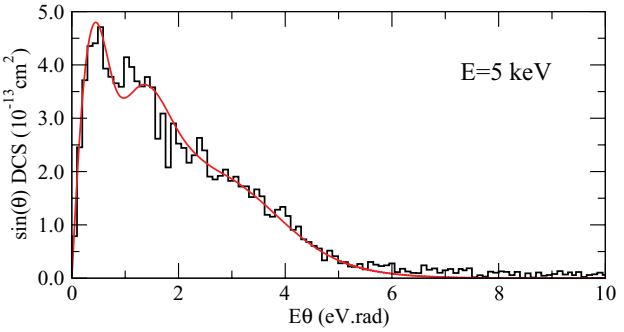

FIG. 18. (Color online) Same as Fig. 11 but for charge transfer from Rb($5p$) to Na($4s$,$3d$,$4p$,$5s$,$4d$) at $E = 5$ keV.

values than in the $Na^+ + Rb(5s)$ case. This is due to the fact that transitions occur at larger impact parameters when the collision is initiated from the Rb($5p$) state, as proved in Fig. 6. The analysis of the collision histories of Figs. 8 and 9 further allowed us to understand the prominent role of rotational redistribution at large R and the concurrent importance of the pseudocrossings of $Na^+ + Rb(5p)$ and $Na(3p) + Rb^+$ molecular curves. As the impact energy is decreased, the system evolves more adiabatically and enters into the region of smaller internuclear distances; inner transitions then occur and yield the secondary maximum of the Na($3p$) DCS at 2 keV. The first maximum, located about $E\theta = 0.2$ eV rad in Fig. 14, is highly structured in the MOCC DCS before convolution; but these oscillatory structures cannot be experimentally resolved.

Figure 15 reports our results for charge transfer from Rb($5p$) to Na($4s$). Theory and experiment agree in providing a DCS which exhibits two main contributions at 2 keV, beyond interference patterns. The first one, peaked at very low $E\theta$, is still visible at $E = 5$ keV; it stems from long-range transitions occurring as the $Na^+ + Rb(5p\sigma)$ and $Na(4s) + Rb^+$ molecular curves pseudocross around $R = 25$ a.u. (see Fig. 5). The second one is much broader and peaked about $E\theta = 3$ eV rad. This outer contribution is also due to radial transitions between the same molecular curves, but at the level of the narrow pseudocrossing located about $R = 11$ a.u. in Fig. 5. Therefore, the second contribution is only accessible at low energies, when the system evolves quite adiabatically in the ingoing part of the collision, and progressively disappears as E increases.

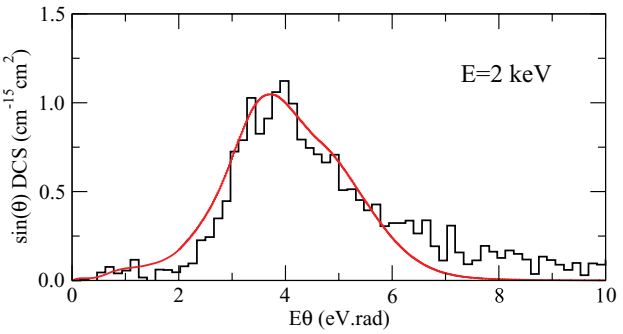

FIG. 17. (Color online) Same as Fig. 11 but for charge transfer from Rb($5p$) to Na($5s$,$4d$,$5p$) at $E = 2$ keV.

$3d$ and $4p$ Na states contribute 19.5% to the total capture flux at 2 keV (see Table V). We accordingly succeeded in deriving a reliable DCS from the measurements, even if we were not able to discriminate between the two levels (see Figs. 3 and 16). In fact, MOCC calculations indicate that 90% of the ($3d + 4p$) capture flux is trapped into the $3d$ shell. The DCS has a lobe shape similar to that of the outer maximum of the $4s$ profile in Fig. 15, with identical locations of maxima. This is due to the fact that a large part of the electron flow that ends up in excited molecular states is initiated by primary radial transitions $Na^+ + Rb(5p\sigma) \rightarrow Na(4s) + Rb^+$ around $R = 11$ a.u. Rotational $Na^+ + Rb(5p\sigma) \rightarrow Na^+ + Rb(4d\pi)$ and radial $Na^+ + Rb(5p\pi) \rightarrow Na^+ + Rb(4d\pi)$ transitions also contribute to this ignition, but they occur in the same $R \sim 10$ a.u. range. The Na($3d$) DCS thus encodes the patterns of prototypical (inner) population of Na($4s$), which has been identified in Fig. 15 to the outer maximum of the $4s$ DCS.

Transitions to even higher excited capture states, $5s$, $4d$, and $5p$, can be distinguished in the Q spectrum of Fig. 3 at 2 keV. The signal is very weak but we nevertheless succeeded in constructing the corresponding DCS from the recoil-ion velocity map; this DCS is presented in Fig. 17 and compared to MOCC results. The agreement is very good, despite the weakness of the signal, because transitions to $4d - 5p$ states occur through promotion of the electronic flux from lower lying states in the $b \geqslant 5$ a.u. range. A remarkable agreement between MOTRIMS and MOCC results is also found in Fig. 18 for capture into excited states at 5 keV; this restores the reliability of our MOCC approach which was undermined in Fig. 13 because of the important role played by inner ($R < 5$ a.u.) transitions in 5-keV $Na^+ + Rb(5s) \rightarrow Na(3d, n \geqslant 4) + Rb^+$ capture collisions.

V. CONCLUSIONS AND PERSPECTIVES

Single charge transfer in low-energy $Na^+ + {}^{87}Rb(5s,5p)$ collisions has been investigated using magneto-optically trapped Rb atoms and high-resolution recoil-ion momentum spectroscopy. Our MOTRIMS setup includes transverse extraction of the recoil ions with 3D electrostatic focusing and fast switch-off of the trapping magnetic field during data counting. This improves both resolution performances and signal over background ratio, thereby making it possible to detect weakly populated charge transfer channels while

dominant processes are measured with improved accuracy (see Tables IV–VI).

We have jointly run semiclassical calculations using the MOCC approach in the framework of the SAE approximation. Special attention has been paid to the description of ionic core screening effects in terms of atom-centered model potentials optimized with effectively complete basis sets. As expected, the calculations reveal diffractionlike patterns in the angular DCSs which are due to the fact that a given capture process occurs in a limited range of impact parameters $b \leqslant b_{\max}$.

Predicted diffractionlike oscillations have been clearly resolved by the experiment (see, e.g., Fig. 10). Following the pioneering work of van der Poel *et al.* [7], this reiterates the advantages of MOTRIMS spectroscopy with respect to conventional scattering geometries which failed in exhibiting such oscillations. Further, our improved setup goes beyond previous MOTRIMS ones which also failed in revealing angular oscillations in the specific case of $Na^+ + Rb$ collisions. However, we note that diffractionlike patterns inherent in some (extremely) long-range capture processes still remain beyond the scope of experiments; for instance, charge transfer from Rb($5p$) to Na($3p$) typically occur within the range $b \lesssim 25$ a.u., which implies a $\sim$64-μrad diffraction spacing between successive angular maxima at $E = 2$ keV, and therefore requires an experimental resolution of $\sim$25 μrad for an unambiguous detection of these maxima. Such a resolution should be reached in the future by using an even lower extraction field.

Besides the experimental evidence of diffractionlike patterns in angular scattering distributions, the MOTRIMS results can be used as a stringent test of the accuracy of theoretical approaches. In the present case, MOCC has made a good job yielding state-selective cross-section ratios and DCS in close agreement with the measurements (see Tables IV–VI and Figs. 11–18). However, the present MOTRIMS measurements have also made it possible to elicit the main shortcoming of any theoretical SAE description using frozen ionic cores (beyond the particular case of present MOCC calculations): Such methods inevitably lead to an inaccurate description of inelastic transitions occurring at small internuclear distances where the projectile and target cores overlap (see Fig. 13); fortunately, such transitions have a (very) small contribution to cross sections [which are built in terms of the opacity functions $bP(b)$] so that an *ab initio* description of core molecularization is useless (at least in systems including long-range transitions; see [45]).

On the basis of the successful complementary of MOTRIMS and MOCC found in the present work, we plan to apply these techniques to the case of oriented and aligned Rb($5p$) initial states. Previous studies using conventional collisional spectroscopies [46,47] were not able to resolve the oscillatory structures and anisotropies appearing in the small scattering angle region. Our MOTRIMS setup is thus the ideal alternative. Furthermore, our improved resolution makes it possible to gauge orientation and alignment effects not only for the most populated capture channel, but also for weakly populated ones.

[1] B. H. Bransden and M. R. C. McDowell, *Charge Exchange and the Theory of Ion-Atom Collisions* (Clarendon, Oxford, 1992).
[2] T. E. Cravens, Science **296**, 1042 (2002).
[3] R. C. Isler, Plasma Phys. Controlled Fusion **36**, 171 (1994).
[4] S. Uehara, L. Toburen, and H. Nikjoo, Int. J. Radiat. Biol. **77**, 139 (2001).
[5] S. Uehara and H. Nikjoo, J. Phys. Chem. B **106**, 11051 (2002).
[6] R. Dörner *et al.*, Phys. Rep. **330**, 95 (2000).
[7] M. van der Poel, C. V. Nielsen, M. A. Gearba, and N. Andersen, Phys. Rev. Lett. **87**, 123201 (2001).
[8] J. W. Turkstra, R. Hoekstra, S. Knoop, D. Meyer, R. Morgenstern, and R. E. Olson, Phys. Rev. Lett. **87**, 123202 (2001).
[9] X. Flechard, H. Nguyen, E. Wells, I. Ben-Itzhak, and B. D. DePaola, Phys. Rev. Lett. **87**, 123203 (2001).
[10] M. van der Poel *et al.*, J. Phys. B **35**, 4491 (2002).
[11] T. G. Lee, H. Nguyen, X. Flechard, B. D. DePaola, and C. D. Lin, Phys. Rev. A **66**, 042701 (2002).
[12] X. Flechard, H. Nguyen, R. Bredy, S. R. Lundeen, M. Stauffer, H. A. Camp, C. W. Fehrenbach, and B. D. DePaola, Phys. Rev. Lett. **91**, 243005 (2003).
[13] H. Nguyen, R. Bredy, H. A. Camp, T. Awata, and B. D. DePaola, Phys. Rev. A **70**, 032704 (2004).
[14] M. Zapukhlyak *et al.*, J. Phys. B **38**, 2353 (2005).
[15] M. H. Shah, H. A. Camp, M. L. Trachy, X. Flechard, M. A. Gearba, H. Nguyen, R. Bredy, S. R. Lundeen, and B. D. DePaola, Phys. Rev. A **72**, 024701 (2005).
[16] S. Knoop, V. G. Hasan, R. Morgenstern, and R. Hoekstra, Phys. Rev. A **73**, 062703 (2006).
[17] J. Blieck *et al.*, Rev. Sci. Instrum. **79**, 103102 (2008).
[18] DL 100 external-cavity diode laser, TOPTICA Photonics AG, http://www.toptica.com.
[19] H. J. Lewandowski *et al.*, J. Low Temp. Phys. **132**, 309 (2003).
[20] E. Liénard *et al.*, Nucl. Instrum. Methods A **551**, 375 (2005).
[21] L. F. Errea *et al.*, J. Phys. B **31**, 3527 (1998).
[22] A. T. Le, C. D. Lin, L. F. Errea, L. Mendez, A. Riera, and B. Pons, Phys. Rev. A **69**, 062703 (2004).
[23] http://www.nist.gov/pml/data/asd.cfm.
[24] B. Pons, Phys. Rev. Lett. **84**, 4569 (2000); Phys. Rev. A **63**, 012704 (2001).
[25] S. Magnier *et al.*, J. Chem. Phys. **98**, 7113 (1993).
[26] http://cdsweb.u-strasbg.fr/topbase/topbase.html.
[27] M. Aymar, S. Azizi, and O. Dulieu, J. Phys. B **36**, 4799 (2003).
[28] L. F. Errea *et al.*, J. Phys. B **32**, L673 (1999).
[29] L. F. Errea *et al.*, J. Phys. B **33**, 3107 (2000).
[30] C. Ghanmi *et al.*, J. Mol. Struct., THEOCHEM **808**, 1 (2007).
[31] Ph. Durand and J. C. Barthelat, Theor. Chim. Acta **38**, 283 (1975).
[32] W. Müller, J. Flesh, and W. Meyer, J. Chem. Phys. **80**, 3279 (1984).
[33] L. F. Errea *et al.*, J. Phys. B **27**, 3603 (1994).
[34] C. Harel and H. Jouin, J. Phys. B **21**, 859 (1988); **25**, 221 (1992).

[35] R. D. Piacentini and A. Salin, Comput. Phys. Commun. **13**, 57 (1977).
[36] M. Abramowitz and I. A. Stegun, *Handbook of Mathematical Functions* (Dover, New York, 1965).
[37] J. Bieck, Ph.D. thesis, University of Caen, France, 2008.
[38] E. C. G. Stueckelberg, Helv. Phys. Acta **5**, 369 (1932).
[39] K. B. MacAdam, J. C. Day, J. C. Aguilar, D. M. Homan, A. D. MacKellar, and M. J. Cavagnero, Phys. Rev. Lett. **75**, 1723 (1995).
[40] D. R. Schultz, C. O. Reinhold, and P. S. Krstić, Phys. Rev. Lett. **78**, 2720 (1997).
[41] P. S. Krstić, C. O. Reinhold, and D. R. Schultz, J. Phys. B **31**, L155 (1998).
[42] R. K. Janev, J. Pop-Jordanov, and E. A. Solov'ev, J. Phys. B **30**, L353 (1997).
[43] P. Botheron and B. Pons, Phys. Rev. A **83**, 062704 (2011).
[44] M. R. C. McDowell and J. P. Coleman, *Introduction to the Theory of Ion-Atom Collisions* (North-Holland, Amsterdam, 1970).
[45] L. F. Errea, F. Guzman, L. Mendez, B. Pons, and A. Riera, Phys. Rev. A **77**, 012706 (2008).
[46] J. W. Thomsen *et al.*, J. Phys. B **32**, 5189 (1999).
[47] D. Dowek *et al.*, J. Phys. B **35**, 2051 (2002).